Chemical Science

ROYAL SOCIETY OF CHEMISTRY

EDGE ARTICLE

View Article Online
View Journal

Cite this: DOI: 10.1039/d6sc01648k

All publication charges for this article have been paid for by the Royal Society of Chemistry

Molecular-level precursor engineering enables high utilization of closed nanopores in hard carbon for sodium-ion batteries

Rui Li, †[a] Beilei Yuan,†[b] Yupeng Feng,[a] Yuhan Li,[a] Na Jiang,[a] Ping Liu,[b] Liangzhi Li,[b] Weiyue Li,[b] Chunwei Dong,*[c] Shuchun Hu,[d] Qi Liu,[a] Jian Chen,*[b] Fei Li,*[e] Jianping Long*[a] and Anjun Hu*[a]

Closed nanopores in hard carbon (HC) are widely regarded as the primary host for low-voltage plateau capacity in sodium-ion batteries, yet their electrochemical inactivity due to poor accessibility remains a critical bottleneck. Here we report a molecular-templating liquid-phase carbonization strategy that engineers biomass precursors with sodium acetate to unlock closed-pore utilization. Sodium acetate simultaneously enriches oxygen-containing functionalities and generates molecular-scale pre-pores during liquid-phase carbonization, enabling controllable closed-pore density and size in bamboo-derived HC. Upon high-temperature treatment, these pre-pores evolve into percolating mesoporous channels that bridge otherwise isolated closed nanopores, thereby constructing an efficient ion-transport network and markedly shortening the solid-state diffusion distance. As a result, the closed-pore utilization reaches 86%, delivering a substantially enhanced plateau contribution together with an expanded interlayer spacing (d_{002} = 0.391 nm). The optimized HC exhibits a high reversible capacity of 369 mA h g^{-1} at 0.1C with 88.9% initial coulombic efficiency, retains ~85% capacity after 500 cycles at 2C, and maintains 257 mA h g^{-1} at −20 °C. This work establishes a molecular-level precursor-engineering route to transform closed pores from "present" to "accessible", providing a general design principle for high-energy HC anodes.

Received 26th February 2026
Accepted 13th April 2026

DOI: 10.1039/d6sc01648k

rsc.li/chemical-science

1. Introduction

Owing to the natural abundance of sodium resources, improved safety, and compatibility with existing lithium-ion battery manufacturing infrastructure, sodium-ion batteries (SIBs) are increasingly considered a strong candidate for large-scale energy storage. Their development is expected to complement and stabilize the lithium-ion battery market and mitigate supply-chain and price volatility through a diversified energy-storage landscape.[1–5] However, the graphite anode used in commercial lithium-ion batteries cannot be directly transferred to SIBs because its narrow interlayer spacing is unfavorable for efficient Na^+ storage. Hard carbon (HC) has therefore emerged as the most promising anode for SIBs due to its low cost, high theoretical capacity, suitable operating potential, and long cycle life.[6,7] Despite this promise, practical HC anodes still suffer from limited reversible capacity, insufficient rate capability, and an incomplete structure–function understanding of sodium storage.

HC is a structurally heterogeneous amorphous/nanocrystalline composite that contains disordered graphene-like microdomains, amorphous regions, surface defects/open pores, and closed nanopores.[6,8] This complexity leads to multiple sodium-storage pathways. The sloping region above ~0.1 V is generally associated with Na^+ adsorption on defect sites and accessible pore surfaces, which usually features fast kinetics and benefits high-rate performance.[9–12] In contrast, the low-voltage plateau below ~0.1 V contributes the majority of capacity in typical HC anodes and is widely linked to sodium storage in the bulk microstructure, including Na^+ insertion/transport within turbostratic domains and pore filling in closed nanopores *via* quasi-metallic Na clustering.[13–15] Recent mechanistic studies have increasingly converged on a three-stage model that integrates these processes, namely Na^+ adsorption at defects and open pores in the sloping region, Na^+

[a]College of Materials and Chemistry & Chemical Engineering (College of Lithium Resources and Lithium Battery Industry), Chengdu University of Technology, Chengdu 610059, China. E-mail: 20066669@chnenergy.com.cn; longjianping@cdut.cn; anjunhu@cdut.edu.cn

[b]Department of Materials Science and Engineering, Sichuan University of Science and Engineering, Zigong 643000, China. E-mail: jchenzg@aliyun.com

[c]National Institute of Clean-and-Low-Carbon Energy, Future Science & Technology City, Changping District, Beijing 102209, China

[d]School of Electronic Engineering, Chengdu Technological University, Chengdu, 611730, China

[e]School of Materials and Energy, University of Electronic Science and Technology of China, Chengdu 611731, China. E-mail: feili@uestc.edu.cn

† These authors contributed equally to this work.

intercalation and transport within turbostratic domains, and pore filling in closed nanopores in the plateau region. This emerging consensus identifies closed nanopores as the primary host of low-voltage capacity. However, a substantial proportion of closed pores remains electrochemically inaccessible because of poor connectivity and long diffusion pathways, resulting in suboptimal utilization of closed-pore capacity.[16–18] Importantly, boosting the sloping capacity through heteroatom doping or defect engineering often increases irreversible reactions and lowers the initial coulombic efficiency (ICE). Accordingly, the rational regulation of closed-pore architecture, particularly strategies that strengthen the plateau contribution while preserving a high ICE, remains a key challenge in the development of advanced HC anodes.[19–21]

Conventional strategies to raise plateau capacity commonly rely on creating abundant open pores through physical/chemical activation and subsequently "closing" them *via* surface reconstruction or secondary carbonization.[22–26] However, these approaches frequently increase closed-pore volume without ensuring electrochemical accessibility. For example, Wang *et al.*[27] reported a fourfold increase in closed-pore volume after chemical activation and high-temperature treatment, yet the plateau capacity increased by only ~1.7 times, implying that a large fraction of closed pores remained inactive. Similarly, Liu *et al.*[28] used P_2O_5 as a sacrificial template/dopant to achieve a 5.4 higher closed-pore volume, but the plateau capacity improved by merely ~1.5 times. In addition to the volume capacity mismatch, activation-derived pores often exhibit broad size distributions and poor structural uniformity, which can limit stable Na clustering and generate tortuous transport pathways that compromise kinetics and rate capability.[29] Collectively, these results underscore a growing bottleneck in which the central task is not simply to produce more closed pores, but to narrow their size dispersion and, more importantly, render them electrochemically accessible so that closed-pore utilization is increased.

Herein, we propose a molecular-templating liquid-phase carbonization strategy to engineer biomass precursors and precisely regulate the density, size, and connectivity of closed nanopores in bamboo-derived HC. Using sodium acetate during liquid-phase carbonization, we simultaneously (i) introduce abundant oxygen-containing functionalities (mainly C=O and C–O) and (ii) generate molecular-scale "pre-pores" within the precursor. Upon high-temperature carbonization, these pre-pores evolve into percolating mesoporous channels that bridge otherwise isolated closed nanopores, establishing an efficient ion-transport network and shortening the effective solid-state diffusion distance for Na^+. Meanwhile, the oxygen-containing groups suppress excessive layer-stacking contraction/graphitization and promote the formation of abundant ultramicropores (<0.8 nm), yielding a closed-pore architecture that is both uniform and highly accessible. As a result, the closed-pore utilization reaches 86%, enabling a markedly enhanced plateau contribution. The optimized sample (SA-BHC) delivers a high reversible capacity of 369 mA h g^{-1} at 0.1C with an ICE of 88.9%, maintains 280 mA h g^{-1} at 2C and 260 mA h g^{-1} at 5C, and retains ~257 mA h g^{-1} even at −20 °C, demonstrating fast kinetics and robust low-temperature operation. This work provides a molecular-level precursor-engineering route to transform closed pores from "present" to "accessible", offering a general design principle for high-energy HC anodes *via* closed-pore utilization.

2. Results and discussion

Optimizing sodium storage in HC hinges on precise regulation of the pore architecture, for which precursor engineering offers a direct handle. Here we synthesize bamboo-derived HC enriched with ultramicropores (SA-BHC) *via* a molecular-templating liquid-phase carbonization strategy. The key concept is to program the precursor with molecular-scale "pre-pores" and oxygenated motifs, so that the final HC contains not only abundant closed nanopores but also improved accessibility/connectivity, which is essential for high closed-pore utilization. Specifically, bamboo powder was hydrothermally treated at 300 °C for 10 h in an aqueous sodium acetate solution. During this process, sodium acetate plays multiple roles: (i) acetic acid generated from hydrolysis catalyzes the depolymerization of lignin and hemicellulose, creating initial pore channels within the precursor; (ii) *in situ* acetate species react with hydroxyl-containing intermediates to form oxygenated functionalities (*e.g.*, ester-related motifs), which subsequently act as molecular-level structure-directing units during condensation/aromatization; and (iii) Na-containing species can further contribute to *in situ* pore formation, collectively enriching the pore network. The resulting precursor is therefore predisposed to evolve into a hierarchical pore system that favors rapid ion transport and efficient sodium storage. For comparison, a hydrothermally carbonized precursor prepared without sodium acetate (Pre-H-BHC) and a precursor obtained by direct pyrolysis of bamboo powder (Pre-D-BHC) were synthesized to clarify the specific structural role of sodium acetate (Fig. 1a).

The chemical structures of the three precursors were first examined by Fourier-transform infrared spectroscopy (FTIR). As shown in Fig. 1b, all samples exhibit characteristic bands near ~3400 cm^{-1} (O–H stretching) and ~920 cm^{-1} (O–C–O-related vibrations), together with a band around ~1600 cm^{-1} associated with aromatic/conjugated carbon frameworks. Notably, Pre-SA-BHC shows markedly stronger absorption in the O–H- and C–O-related regions than Pre-H-BHC and Pre-D-BHC, indicating that sodium-acetate-assisted liquid-phase carbonization introduces more abundant oxygen-containing functional groups.[30–32] X-ray photoelectron spectroscopy (XPS) further supports this conclusion. The survey spectra (Fig. S1) confirm the presence of C and O in all precursors, with Pre-SA-BHC exhibiting a higher oxygen content than Pre-D-BHC. Deconvolution of the C 1s spectra (Fig. 1c) yields peaks at 284.8 eV (C–C/C=C), 286.5 eV (C–O), and 288.6 eV (carbonyl/ester-related O–C=O), consistent with an oxygen-enriched precursor structure.[33] The relative contribution of the oxygenated components (especially the higher-binding-energy peak) is substantially enhanced in Pre-SA-BHC compared with Pre-H-BHC and Pre-D-BHC (Fig. 1c and S2). In addition, O 1s spectra (Fig. 1d) can be fitted with two components at 531.5 eV

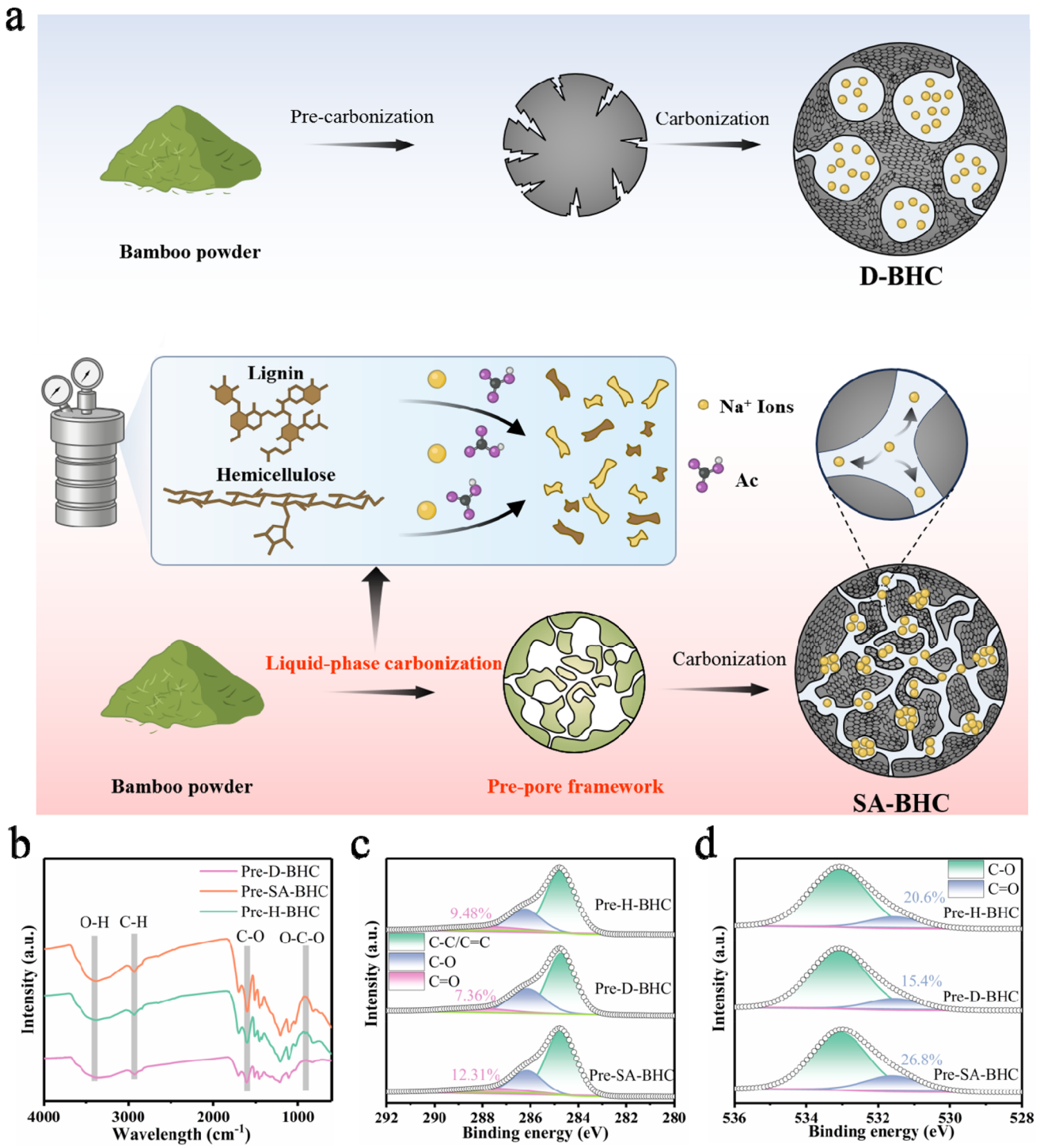

Fig. 1 (a) Schematic illustration of the molecular-templating liquid-phase carbonization process. (b) FTIR spectra of Pre-H-BHC, Pre-SA-BHC, and Pre-D-BHC. (c) High-resolution C 1s XPS spectra of Pre-H-BHC, Pre-SA-BHC, and Pre-D-BHC. (d) High-resolution O 1s XPS spectra of Pre-H-BHC, Pre-SA-BHC, and Pre-D-BHC.

and 533.0 eV, assigned to C═O and C–O, respectively. Quantitatively, the fraction of C═O in Pre-SA-BHC reaches 26.8%, exceeding that in Pre-H-BHC (20.6%) and Pre-D-BHC (15.4%) (Fig. S2). These results indicate that sodium acetate effectively introduces abundant carbonyl-related motifs, which are expected to exert a molecular-templating effect and favor ultramicropore development during subsequent high-temperature carbonization.[33]

The thermal stability and carbonization behavior of the precursors were evaluated by thermogravimetric analysis (TGA). Compared with Pre-D-BHC (char yield: 50.2%), Pre-SA-BHC exhibits a higher char yield (53.3%), suggesting improved

thermal stability enabled by the liquid-phase carbonization route (Fig. S3). Such enhanced stability can suppress premature volatilization and excessive surface-defect generation during carbonization, which is beneficial for improving the ICE of the resulting HC. In the low-temperature region (up to ~215 °C), Pre-SA-BHC shows a lower mass-loss rate than Pre-D-BHC, consistent with more stabilized aromatic/conjugated structures. During the major weight-loss stage around ~400 °C, Pre-SA-BHC still exhibits a lower mass-loss rate, implying a more robust carbon skeleton. This stability provides a favorable basis for forming a more uniform internal pore structure upon high-temperature treatment. The degree of crosslinking in the precursors was further assessed *via* ethanol-insoluble content measurements (Fig. S4). Pre-SA-BHC shows a lower insoluble fraction than Pre-H-BHC, indicating reduced crosslinking density.[34] This difference is plausibly associated with acetate-involved reactions that alter the polymerization/condensation pathway of hydrolysis products, thereby promoting the formation of molecular-scale free volume in the precursor. These pre-pores are expected to act as structural seeds for the evolution of closed nanopores in the final HC.[34]

The microstructures of the three HC samples were examined by high-resolution transmission electron microscopy (HRTEM) (Fig. 2a–c). D-BHC shows relatively extended, locally ordered layer stacking, indicative of a higher degree of graphitization, while internal nanopores are scarce and heterogeneously distributed. For H-BHC, the pore population increases and layer ordering is suppressed; however, the carbon domains remain comparatively large and the pore size distribution appears broad. In contrast, SA-BHC exhibits typical short-range ordering with highly distorted/turbostratic layer arrangements and a large number of uniformly dispersed ultramicropores, indicating that the molecular-templating liquid-phase carbonization effectively regulates both the disorder degree and the pore nucleation uniformity within the carbon framework.

The crystallographic features were further analyzed by X-ray diffraction (XRD) (Fig. 2d). All samples display broad reflections centered at ~23.6° and ~43.6°, corresponding to the (002) and (100) planes of turbostratic carbon, respectively.[35,36] Compared with D-BHC, the (002) peak of SA-BHC shifts to a lower angle, indicating expanded interlayer spacing. The d_{002} value calculated using Bragg's law reaches 0.391 nm for SA-BHC, larger than those of H-BHC (0.383 nm) and D-BHC (0.372 nm), consistent with the HRTEM observations. In addition, the stacking height (L_c) of SA-BHC is 1.38 nm, exceeding that of H-BHC (1.21 nm) and D-BHC (0.98 nm) (Table S1). Together with the broadened diffraction features, these results suggest that liquid-phase carbonization promotes a more turbostratic, defect-rich nanodomain structure that is favorable for generating internal free volume and nanopores. Deconvolution of the (002) peak (Fig. S5) further reveals a higher fraction of turbostratic components in SA-BHC, indicating a more disordered internal structure.[36]

Raman spectroscopy was employed to further resolve defect-related structural evolution (Fig. 2e). The spectra were deconvoluted into four contributions (D1, D2, D3, and G).[31] SA-BHC exhibits the highest I_{D2}/I_G ratio (0.89) (Fig. S6 and Table S2), indicating the highest density of defect-related features that can contribute to reversible Na^+ adsorption and rapid interfacial kinetics.[37] Moreover, SA-BHC shows the smallest lateral domain size (L_a = 6.36 nm), reflecting reduced graphitic domain coherence and enhanced short-range order. The biphasic domain structure, consisting of disordered turbostratic domains and graphitic nanodomains, as revealed by XRD deconvolution (Fig. S5) and Raman fitting (Fig. S6), is closely correlated with the three-stage sodium storage mechanism. The disordered domains provide abundant defect sites and open pores, thereby favoring Na^+ adsorption in the sloping region, whereas the graphitic nanodomains, with an expanded interlayer spacing of up to 0.391 nm for d_{002}, facilitate Na^+ intercalation and transport. Notably, SA-BHC exhibits the highest proportion of disordered domains, which promotes the formation of closed nanopores and thereby accounts for its superior plateau capacity. Consistently, XPS C 1s fitting (Fig. S7) reveals an increased sp^3-C fraction in SA-BHC relative to D-BHC, which correlates with a higher density of bulk defects. These bulk defects can serve as internal transport shortcuts and help reduce ion-transport tortuosity, thereby facilitating access to pore interiors and improving rate capability.[38]

The pore architecture was evaluated by N_2 adsorption–desorption measurements (Fig. 2g). All samples display type I isotherms, indicating predominantly microporous characteristics.[39] The BET specific surface areas of D-BHC, H-BHC, and SA-BHC are 32.7, 21.1, and 24.3 $m^2\ g^{-1}$, respectively (Fig. 2g and Table S3). SA-BHC exhibits the highest micropore volume (0.00966 $cm^3\ g^{-1}$), with pore sizes mainly distributed in the 1.4–2.0 nm range (Fig. 2h). D-BHC exhibits the highest surface area, likely because its direct pyrolysis route tends to generate abundant open pores and surface defects. Such a high surface area may expose more carbon edge sites to the electrolyte, thereby promoting SEI formation and irreversible Na^+ consumption, which can adversely affect the ICE. In contrast, the hydrothermal pretreatment used for H-BHC and SA-BHC produces a more compact carbon framework with a lower surface area. The slightly higher surface area of SA-BHC compared with H-BHC is attributed to the etching effect of sodium acetate during liquid-phase carbonization, which creates additional microchannels and improves pore connectivity. This optimized pore structure may further facilitate electrolyte wetting and ion transport, as will be examined in greater detail through electrochemical characterization. To probe ultramicroporosity (<1 nm), CO_2 adsorption was conducted (Fig. 2i). Herein, ultramicropores are defined as pores smaller than 1 nm, as determined by CO_2 adsorption measurements. SA-BHC shows a markedly higher ultramicropore volume concentrated in the 0.45–0.85 nm range compared with H-BHC and D-BHC. This enrichment of size-matched ultramicropores provides a favorable confined environment for low-voltage sodium storage and can improve effective ion transport within the carbon matrix.

Because gas adsorption primarily reflects accessible (open) porosity, small-angle X-ray scattering (SAXS) was further employed to probe the closed-pore characteristics (Fig. 2j). In this work, closed nanopores are defined as pores inaccessible to

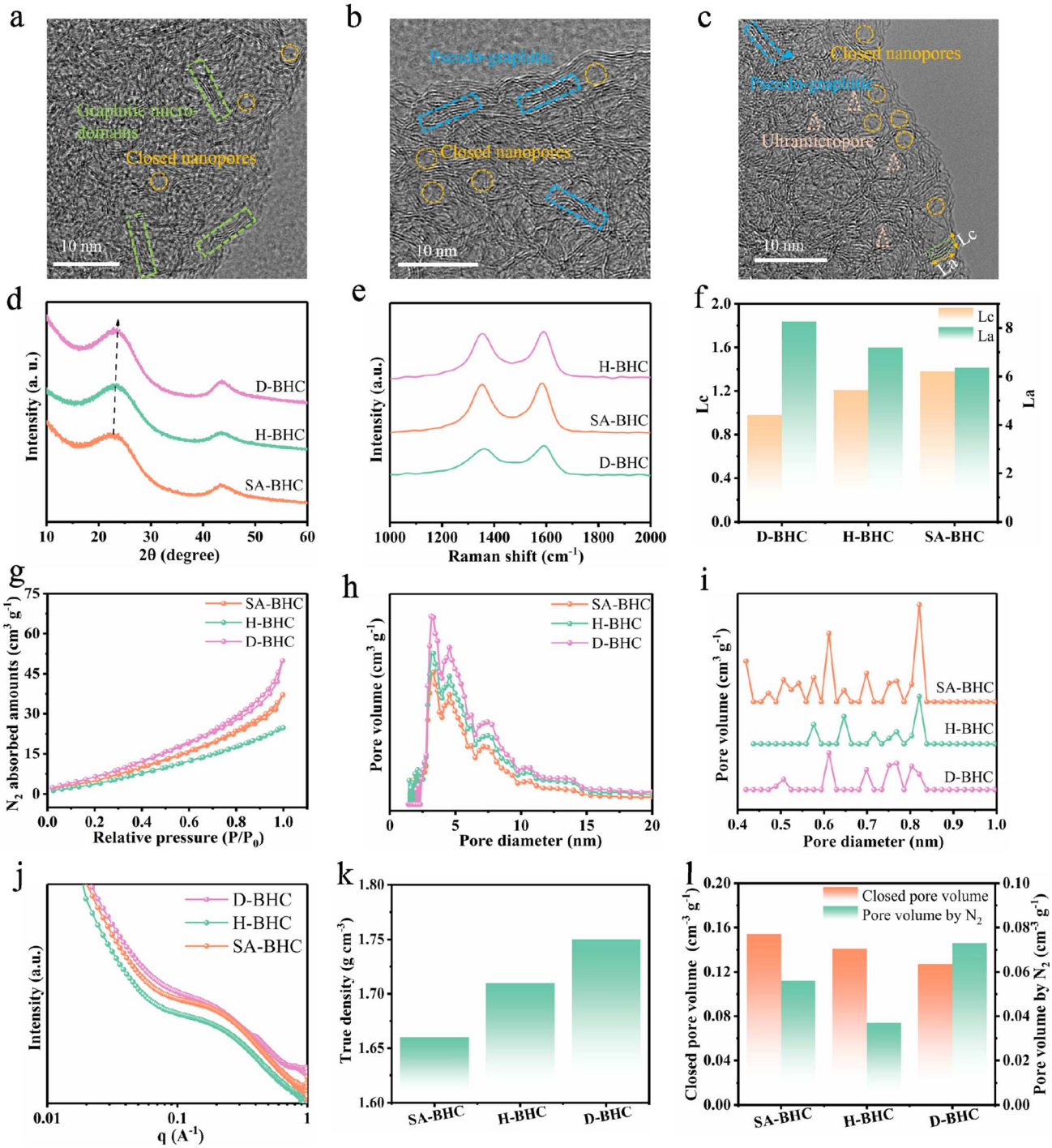

Fig. 2 (a–c) HRTEM images of D-BHC, H-BHC, and SA-BHC. (d) XRD patterns. (e) Raman spectra. (f) Lateral crystallite size (L_a) and stacking height (Lc) of D-BHC, H-BHC, and SA-BHC. (g) N_2 adsorption–desorption isotherms. (h) Pore-size distributions derived from N_2 adsorption. (i) Ultramicropore-size distributions derived from CO_2 adsorption. (j) SAXS profiles. (k) True density. (l) Closed-pore volume estimated from true-density measurements.

N_2 and therefore undetectable by gas adsorption, but identifiable and quantifiable by SAXS and true density measurements. SA-BHC presents a discernible shoulder near ~0.1 $Å^{-1}$, indicative of an increased population of closed nanopores relative to H-BHC and D-BHC.[40] The extracted characteristic closed-pore diameters for D-BHC, H-BHC, and SA-BHC are 2.56, 2.43, and 2.21 nm, respectively (Fig. S8, S9 and Table S3), suggesting that the proposed strategy favors the formation of smaller and more densely distributed closed nanopores. Consistently, true-density measurements (Fig. 2k and l) show that SA-BHC has the lowest true density (1.68 g cm^{-3}) and the highest closed-pore volume, in agreement with the SAXS-derived trends.

Taken together, these analyses show that molecular-templated liquid-phase carbonization enables coordinated control of both open and closed porosity while strongly favoring ultramicropore formation, thereby providing a structural foundation for improved low-voltage storage and for higher closed-pore utilization in subsequent electrochemical evaluations.

To systematically evaluate sodium-storage behavior, half-cells were assembled with sodium metal as the counter/reference electrode. Cyclic voltammetry (CV) at 0.1 mV s^{-1} (Fig. 3a) shows a broad cathodic feature at ~0.3–0.5 V for D-BHC, consistent with pronounced Na^+ uptake dominated by surface/defect-related adsorption processes. In contrast, SA-BHC exhibits sharper redox features concentrated near ~0.1 V, suggesting that its confined pore structure contributes more significantly to low-voltage storage.[41,42] Galvanostatic charge–discharge profiles at 0.1C (Fig. 3b, S10a and b) display the characteristic sloping region above ~0.1 V and a plateau below ~0.1 V for all samples. While the sloping capacities are comparable, SA-BHC delivers a markedly higher first-discharge capacity of 408.4 mA h g^{-1} and a plateau capacity of 275 mA h g^{-1}, outperforming H-BHC (341 mA h g^{-1}; 227 mA h g^{-1}) and D-BHC (288 mA h g^{-1}; 211 mA h g^{-1}) (Fig. 3c, S10a and b). Because the plateau region is closely associated with storage in confined and closed pores, these results suggest that molecular-templated liquid-phase carbonization does not simply increase porosity, but instead activates a larger fraction of the pore volume by improving pore uniformity and accessibility, which raises closed-pore utilization and strengthens the plateau contribution. Notably, SA-BHC achieves a high ICE of 88.9%, substantially higher than that of D-BHC (74.0%), implying suppressed irreversible reactions and more stable interfacial chemistry enabled by the optimized microstructure. Overall, the enhanced plateau capacity in SA-BHC aligns with its enriched ultramicropore population, highlighting size-matched ultramicropores as key hosts for low-voltage sodium storage.

Rate capability was further evaluated from 0.1C to 5C (Fig. 3d,e). As the rate increases from 0.1C to 5C, the discharge capacity of D-BHC drops sharply from 291 to 125 mA h g^{-1}. In contrast, SA-BHC shows much better retention, decreasing only from 369 to 260 mA h g^{-1}. When the current is returned to 0.1C, the capacities recover to 278 mA h g^{-1} (D-BHC) and 343 mA h g^{-1} (SA-BHC), respectively, indicating good structural reversibility for SA-BHC under high-rate cycling. Four-probe measurements under various pressures further confirm that the excellent rate performance and conductivity mainly originate from the uniformly distributed and highly efficient graphitic nanodomains (Fig. S11). Importantly, charge–discharge curves at different rates (Fig. 3e, S10c and d) reveal that even at 5C, SA-BHC maintains a plateau capacity of 159 mA h g^{-1}, significantly higher than those of H-BHC (107 mA h g^{-1}) and D-BHC (80 mA h g^{-1}) (Fig. S12). This improved high-rate plateau retention is consistent with the presence of percolating ion-transport pathways generated during sodium-acetate-assisted liquid-phase carbonization, which reduce transport tortuosity and facilitate access to confined storage sites. Compared with reported bamboo-derived HC anodes, SA-BHC exhibits clear advantages in both reversible capacity and ICE (Fig. 3f and Table S4).

Long-term cycling performance was assessed at 2C (Fig. 3g). After 500 cycles, SA-BHC retains 87.5% of its capacity, substantially higher than H-BHC (68.3%) and D-BHC (59.2%). Variable-scan-rate CV (Fig. S13) and kinetic analysis (Fig. S14 and S15) show that the capacitive contribution of SA-BHC increases from 57% at 0.1 mV s^{-1} to 92% at 1.0 mV s^{-1}, indicative of fast surface/near-surface-controlled kinetics that benefit high-rate operation. Practical electrode-loading tests further demonstrate that SA-BHC maintains ~220 mA h g^{-1} at 5C at both low (~1.5 mg cm^{-2}) and high (~2.6 mg cm^{-2}) loadings (Fig. S16 and S17). Under high loading, it still delivers 212 mA h g^{-1} after 250 cycles at 5C (Fig. S18), supporting its practical viability.

The combination of uniform ultramicropores (providing abundant confined storage sites) and *in situ*-formed transport pathways (improving accessibility to these sites) synergistically enhances closed-pore utilization and ion-transport kinetics, leading to rate capability and cycling stability that compare favorably with many reported HC anodes.[15–19,26–32] Furthermore, low-temperature tests (Fig. 3h–j) highlight the robustness of this architecture. At −20 °C and 0.1C, SA-BHC delivers a plateau capacity of 220 mA h g^{-1}, higher than that of D-BHC (154 mA h g^{-1}). Even at 2C under −20 °C, SA-BHC maintains 150 mA h g^{-1}, significantly outperforming D-BHC (85 mA h g^{-1}), indicating that the optimized pore accessibility and shortened transport length help preserve pore-filling kinetics under sluggish low-temperature conditions.

To gain deeper insight into reaction kinetics, *in situ* electrochemical impedance spectroscopy (EIS) was performed for D-BHC and SA-BHC during sodiation/desodiation (Fig. 4a and S19). SA-BHC consistently exhibits lower impedance than D-BHC throughout the entire potential window, indicating faster overall charge-transfer/ion-transport processes. Notably, the impedance of SA-BHC varies only mildly with potential, which is consistent with the formation of a relatively stable, thin, and uniform interphase at the electrode/electrolyte interface and is expected to benefit long-term cycling stability.[43]

Bulk Na^+ transport was further evaluated by galvanostatic intermittent titration technique (GITT) (Fig. 4b). While the three electrodes display similar overall GITT profiles, indicating broadly comparable storage stages, the apparent diffusion coefficient (D_a) exhibits clear voltage-dependent differences. In the mid-voltage region (~1.0–0.5 V), all samples exhibit an initial increase followed by a decrease in D_a, which is plausibly associated with interphase formation and concurrent surface reactions. At intermediate potentials, the fluctuations in D_a reflect a combination of defect/surface adsorption and transport within turbostratic microdomains. Importantly, in the low-potential region (0.04–0 V), D_a increases continuously, consistent with the onset of pore-filling-dominated behavior.[44,45] Across the entire voltage window, SA-BHC shows a systematically higher D_a than D-BHC, indicating accelerated Na^+ transport both at the interface and within the carbon matrix. Taken together with the *in situ* EIS results, these observations suggest that the precursor-engineered architecture of SA-BHC, including internal transport shortcuts and reduced tortuosity, improves access to confined storage sites and thereby supports faster kinetics and higher effective utilization of closed pores.

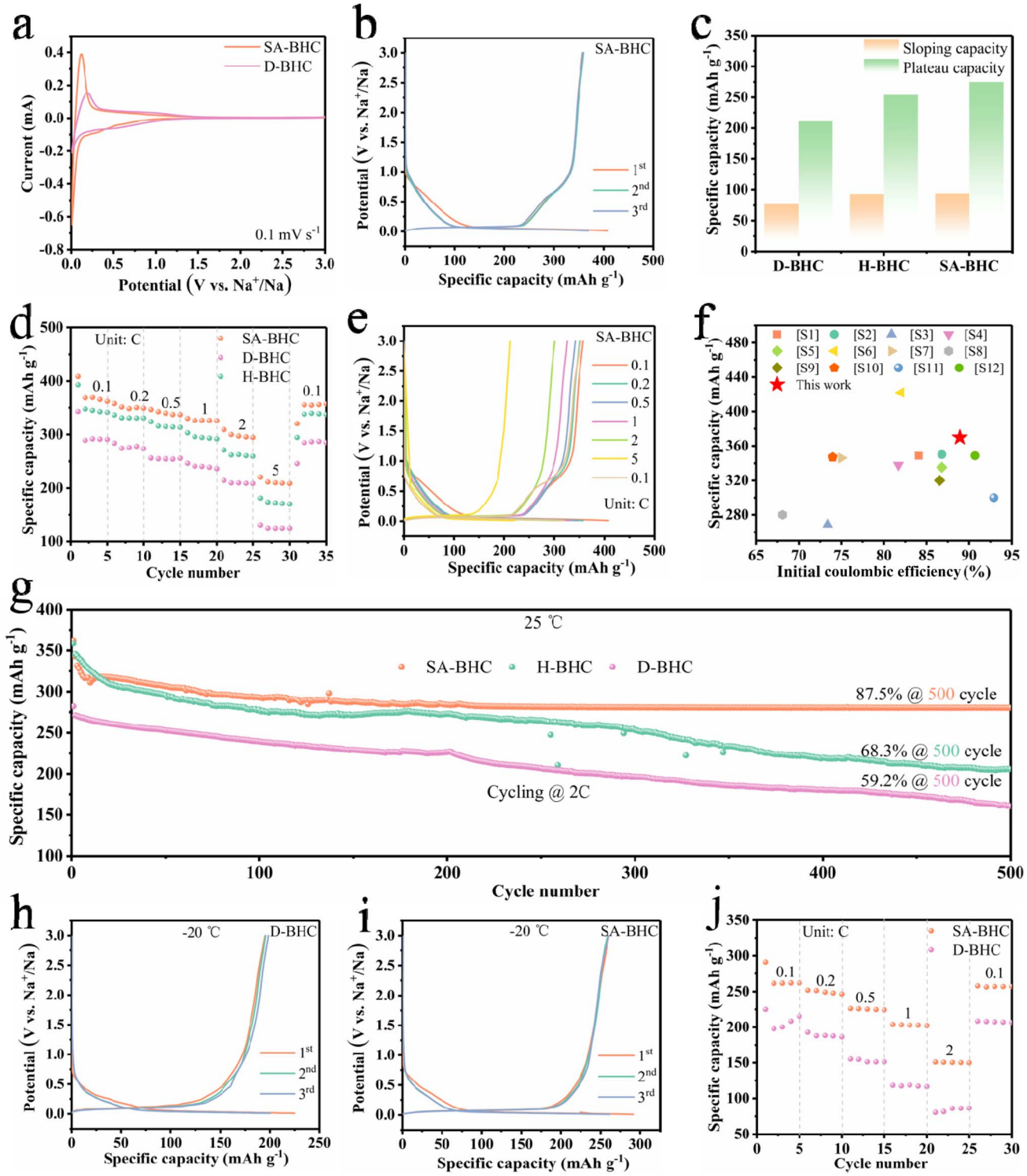

Fig. 3 (a) CV curves of D-BHC and SA-BHC at 0.1 mV s^{-1}. (b) GCD profiles of SA-BHC at 0.1C. (c) Comparison of slope and plateau capacities among D-BHC, H-BHC, and SA-BHC. (d) Rate performance from 0.1 to 5C. (e) GCD profiles of SA-BHC at rates from 0.1 to 5C. (f) Comparison of the reversible capacity and ICE of SA-BHC with those of reported bamboo-derived HC anodes for SIBs. (g) Long-term cycling performance at 2C. (h, i) GCD profiles of D-BHC and SA-BHC at 0.1C measured at room temperature and −20 °C. (j) Rate capability of D-BHC and SA-BHC at −20 °C.

To elucidate the sodium-storage mechanism in SA-BHC, we combined *ex situ* XPS with *in situ* Raman spectroscopy and *in situ* XRD. *Ex situ* Na 1s XPS (Fig. 4c) shows that a distinct Na signal appears upon discharging to 0.15 V, indicating desolvation and initial Na^+ uptake into the carbon framework. When discharged to 0.01 V, the Na 1s peak shifts to 1071.4 eV, implying a modified electronic environment for sodium consistent with quasi-metallic Na confined in nanopores.[46]

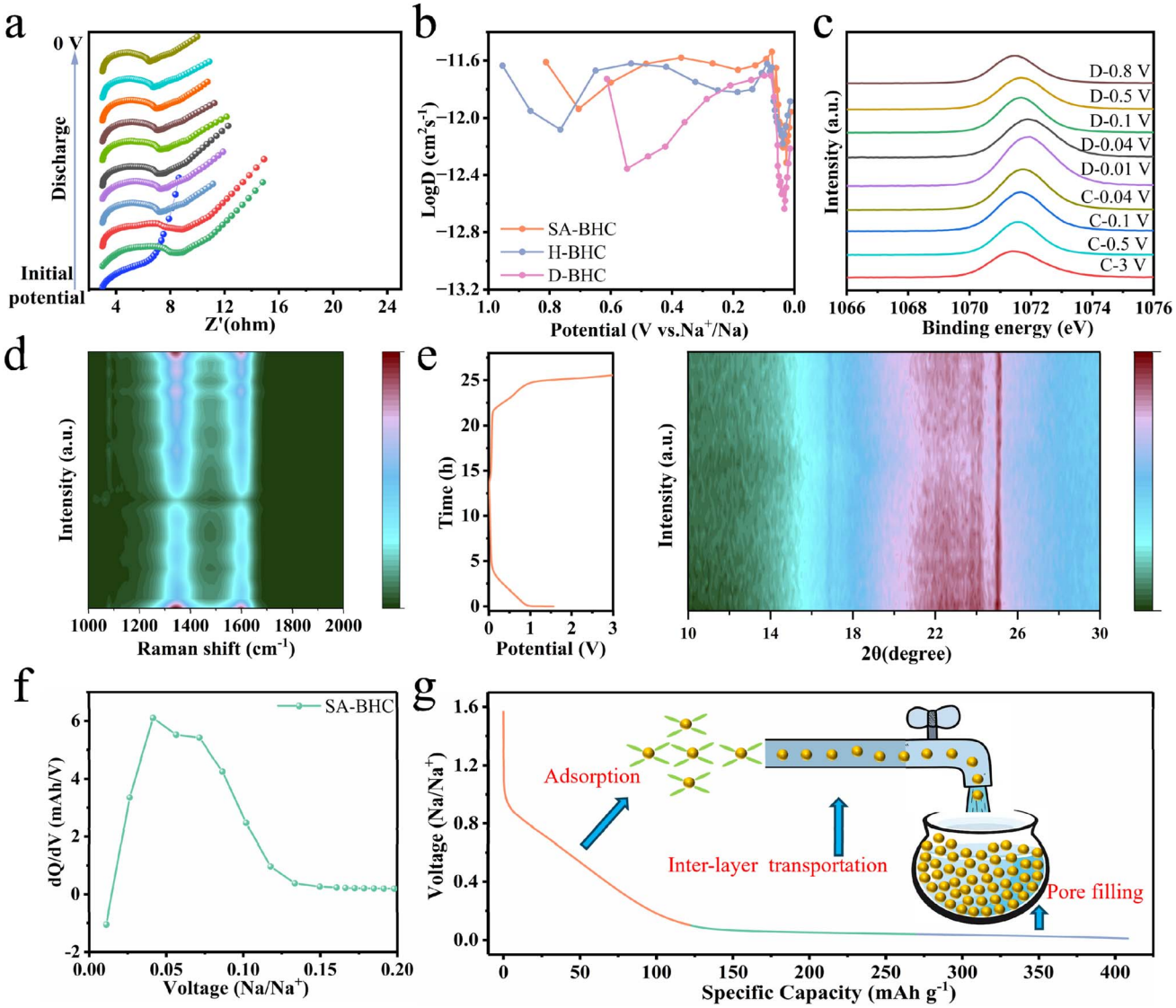

Fig. 4 (a) *In situ* EIS of the SA-BHC electrode during the discharge (sodiation) process. (b) GITT profiles of D-BHC, H-BHC, and SA-BHC. (c) *Ex situ* high-resolution Na 1s XPS spectra at selected states of charge. (d) *In situ* Raman spectra of the SA-BHC electrode during the first charge/discharge. (e) *In situ* XRD patterns of the SA-BHC electrode during the first charge/discharge. (f) Capacity differential (d*Q*/d*V*) curves of SA-BHC. (g) Schematic illustration of the sodium-storage stages in the SA-BHC anode.

Upon charging, the peak reversibly returns to 1071.2 eV, indicating good reversibility of the stored sodium species. Notably, the Na 1s position remains essentially stable upon charging to 3.0 V, suggesting that the dominant sodium species associated with adsorption/transport processes does not undergo an obvious valence-state transition within this window.

In situ Raman spectroscopy provides complementary evidence for the low-voltage storage evolution (Fig. 4d). At potentials above ~0.1 V, the D and G bands show only minor changes. In contrast, below ~0.15 V, the D-band intensity decreases markedly and the G band redshifts accompanied by intensity attenuation. These changes can be attributed to electron injection associated with Na uptake into the π* states of graphitic microdomains, which weakens C–C bond vibrations and reflects increased electronic interaction between Na and the carbon framework. The persistent G-band redshift at low potentials is consistent with progressive electron transfer and the formation of quasi-metallic Na clusters in confined spaces.[47] Such quasi-metallic clustering is favored only when the pore size provides sufficient confinement and stabilization, underscoring why engineering size-matched ultramicropores is central to achieving high closed-pore utilization. The Raman signals recover well upon charging, supporting the structural stability and reversibility of SA-BHC during cycling.

In situ XRD further clarifies the structural response during cycling (Fig. 4e). No pronounced (002) peak shift/breathing is observed, suggesting that intercalation-induced staging is not the dominant storage mode; instead, low-voltage storage is more plausibly governed by pore filling together with defect-related uptake.[36] Consistently, the differential capacity (d*Q*/d*V*)

curve (Fig. 4f) shows two clear inflection features below 0.2 V, located near ~0.15 V and ~0.04 V, indicating transitions between distinct storage regimes. Guided by these inflections and the quasi-metallic Na evidence, we assign the 0.04–0.01 V window to the pore-filling-dominated process. To further validate the formation of reactive, quasi-metallic Na, electrodes discharged to 0.01 V were immersed in 1 wt% phenolphthalein ethanol solution. The D-BHC electrode induces negligible color change, whereas the SA-BHC electrode turns the solution a distinct purple-red (Fig. S20a), providing visual evidence for a higher amount of quasi-metallic Na species in SA-BHC. Moreover, SA-BHC electrodes harvested at different potentials show progressively intensified coloration with decreasing voltage and reversible fading upon charging, consistent with the reversibility of the low-voltage storage process (Fig. S20b).

Based on these complementary results, the sodium-storage behavior of SA-BHC can be summarized as a three-stage "adsorption-transport-pore filling" mechanism (Fig. 4g): from open-circuit voltage to ~0.15 V, Na^+ is mainly stored *via* adsorption at defects/surface-accessible sites; from ~0.15 to ~0.04 V, Na^+ transport/uptake within turbostratic microdomains becomes prominent; and from ~0.04 to 0 V, Na fills closed nanopores to form quasi-metallic clusters. Accordingly, closed-pore utilization is quantified as follows:

$$Q_{\text{pore,theoretical}} = V_{\text{closed}} \times C_{\text{v,Na}} \quad (1)$$

$$\text{Closed-pore utilization} = Q_{\text{plateau}}\,(0.01\text{–}0.04\ \text{V})/Q_{\text{pore,theoretical}} \quad (2)$$

where $C_{\text{v, Na}}$ is the theoretical volumetric capacity of sodium metal (1128 mA h cm^{-3}), V_{closed} is the closed-pore volume obtained from true-density measurements, and Q_{plateau} (0.01–0.04 V) is the plateau capacity within the pore-filling-dominated window defined above. The calculated closed-pore utilizations for D-BHC, H-BHC, and SA-BHC are 71%, 79%, and 86%, respectively (Fig. S21). These values quantitatively confirm that molecular-templating liquid-phase precursor engineering enhances not only the presence of closed pores but, more importantly, their electrochemical accessibility and utilization.

To rationalize the enhanced closed-pore utilization at the atomic scale, we constructed a representative closed-pore model consisting of two cross-linked defective carbon layers (Fig. 5a) and carried out systematic calculations. The evolution of the average potential during stepwise Na filling inside the pore (Fig. 5b) shows a pronounced decrease as the number of Na atoms increases. Specifically, when the Na number increases from 1 to 3, the average potential rapidly approaches ~0 V; when the number reaches 9, the potential further shifts to negative values.[2] This trend is consistent with a mechanistic picture in which higher-potential capacity is mainly associated with defect-mediated adsorption/uptake and near-surface transport, whereas cluster-like Na accumulation (pore filling) becomes thermodynamically favorable only in the low-potential region, corresponding to the plateau in the electrochemical profiles.

We then calculated Na^+ diffusion barriers between carbon layers with different interlayer spacings (Fig. 5c). The diffusion penalty is substantial when the spacing falls within 0.36–0.38 nm, while the barrier decreases markedly once the spacing exceeds ~0.38 nm and then becomes less sensitive to further expansion. Furthermore, we evaluated the energetics of Na filling in pores with different characteristic sizes (Fig. 5d). For pores larger than ~2 nm, the binding energy remains relatively high and shows weak size dependence. In contrast, when the pore size decreases below ~1 nm, the binding energy drops sharply, indicating that pores in the 0.5–1.0 nm range are more favorable for stabilizing confined Na species and enabling efficient low-voltage pore filling.[14] Combining this theoretical preference with CO_2 adsorption results (Fig. 2i), SA-BHC exhibits an ultramicropore population concentrated within the optimal 0.45–0.85 nm range, whereas D-BHC shows a broader and less uniform distribution. This alignment between theory and experiment provides a mechanistic explanation for the higher plateau capacity of SA-BHC and further supports the role of molecular-templating liquid-phase precursor engineering in promoting size-matched ultramicropores and improving closed-pore utilization.

Beyond bulk storage, interphase chemistry is critical for realizing high ICE and fast kinetics. To elucidate the interfacial origin of the superior electrochemical performance of SA-BHC, electrodes after 500 cycles were systematically examined. HRTEM images (Fig. 5e and S22) reveal that SA-BHC forms a uniform and ultrathin solid electrolyte interphase (SEI) of ~10 nm, consistent with reduced continuous electrolyte decomposition and contributing to its high ICE (88.9%). Such a thin yet compact SEI can shorten the interfacial transport length for Na^+ and mitigate polarization. In contrast, the SEI on D-BHC is thicker and more heterogeneous (Fig. 5g), indicative of more severe parasitic reactions and electrolyte consumption, consistent with its lower ICE (~73%). Although SA-BHC already shows a markedly improved ICE relative to the control samples, further gains may still be achievable through electrolyte/additive/binder optimization.[48–51]

Time-of-flight secondary ion mass spectrometry (TOF-SIMS) was employed to further resolve the SEI composition and spatial distribution (Fig. 5f and h). Depth profiles of representative fragments, including an inorganic species NaF_2^- and organic species $C_3H_5O_3^-$ and CH_3COO^-, reveal a much stronger NaF_2^- signal for SA-BHC than for D-BHC, indicating a larger inorganic contribution to the SEI. In contrast, D-BHC exhibits stronger organic fragment signals, particularly toward the inner SEI region, suggesting an SEI richer in organic decomposition products. Such organic-dominated SEI typically correlates with sustained electrolyte decomposition and poorer ion-transport properties, which can accelerate performance decay.

To further resolve the chemical composition and spatial distribution of the SEI, depth-resolved XPS was conducted on cycled electrodes (Fig. 6a–d). The evolution of elemental signals and atomic ratios with sputtering time reveals a clear compositional gradient across the SEI, consistent with a layered interphase structure. In the O 1s depth profiles, the C–O-related contribution for SA-BHC decreases noticeably with increasing etching time, which is consistent with a comparatively thinner and/or less decomposed SEI containing a smaller fraction of carbonate-like species (*e.g.*, Na_2CO_3). In contrast, D-BHC shows

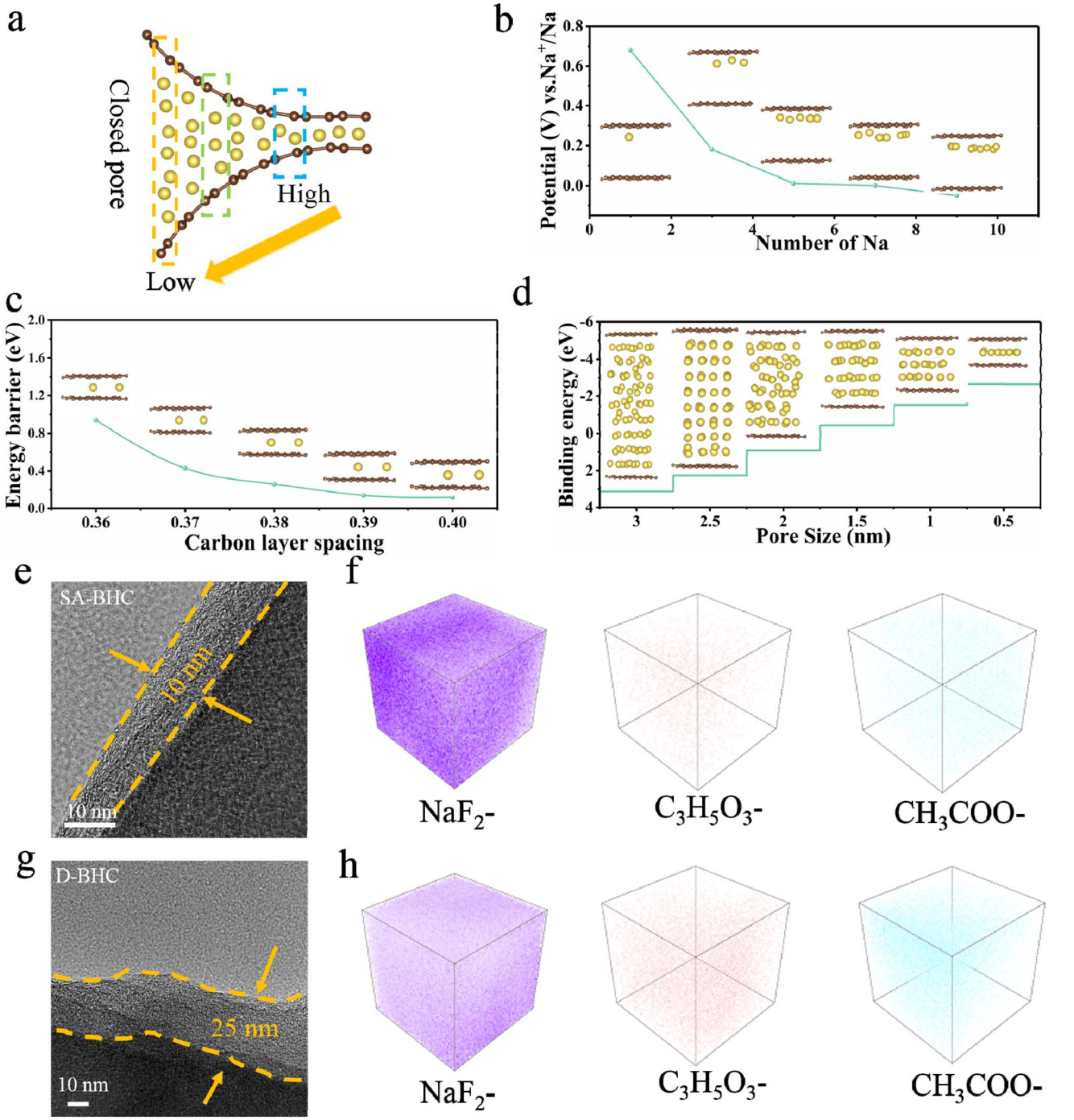

Fig. 5 (a) Schematic closed-pore model used for theoretical calculations. (b) Evolution of average potential during stepwise Na filling and corresponding optimized configurations. (c) Calculated Na^+ diffusion barriers as a function of carbon interlayer spacing. (d) Energetics of Na filling as a function of pore size. (e and g) HRTEM images of the SEI on SA-BHC (e) and D-BHC (g) electrodes after cycling. (f and h) 3D TOF-SIMS reconstructions showing the spatial distributions of representative inorganic and organic species in the SEI on SA-BHC (f) and D-BHC (h).

persistently strong oxygen-related signals throughout the sputtering sequence, indicative of more extensive electrolyte decomposition products distributed across the SEI thickness.

The F 1s spectra provide additional insight into SEI chemistry. Characteristic components assigned to C–F and Na–F are observed at ~685.7 and ~690.3 eV, respectively, confirming that the SEI contains both organic and inorganic fluorinated species. Importantly, the relative fraction of inorganic components (particularly NaF, together with Na_2O/oxygen-containing inorganic species) is higher for SA-BHC than for D-BHC

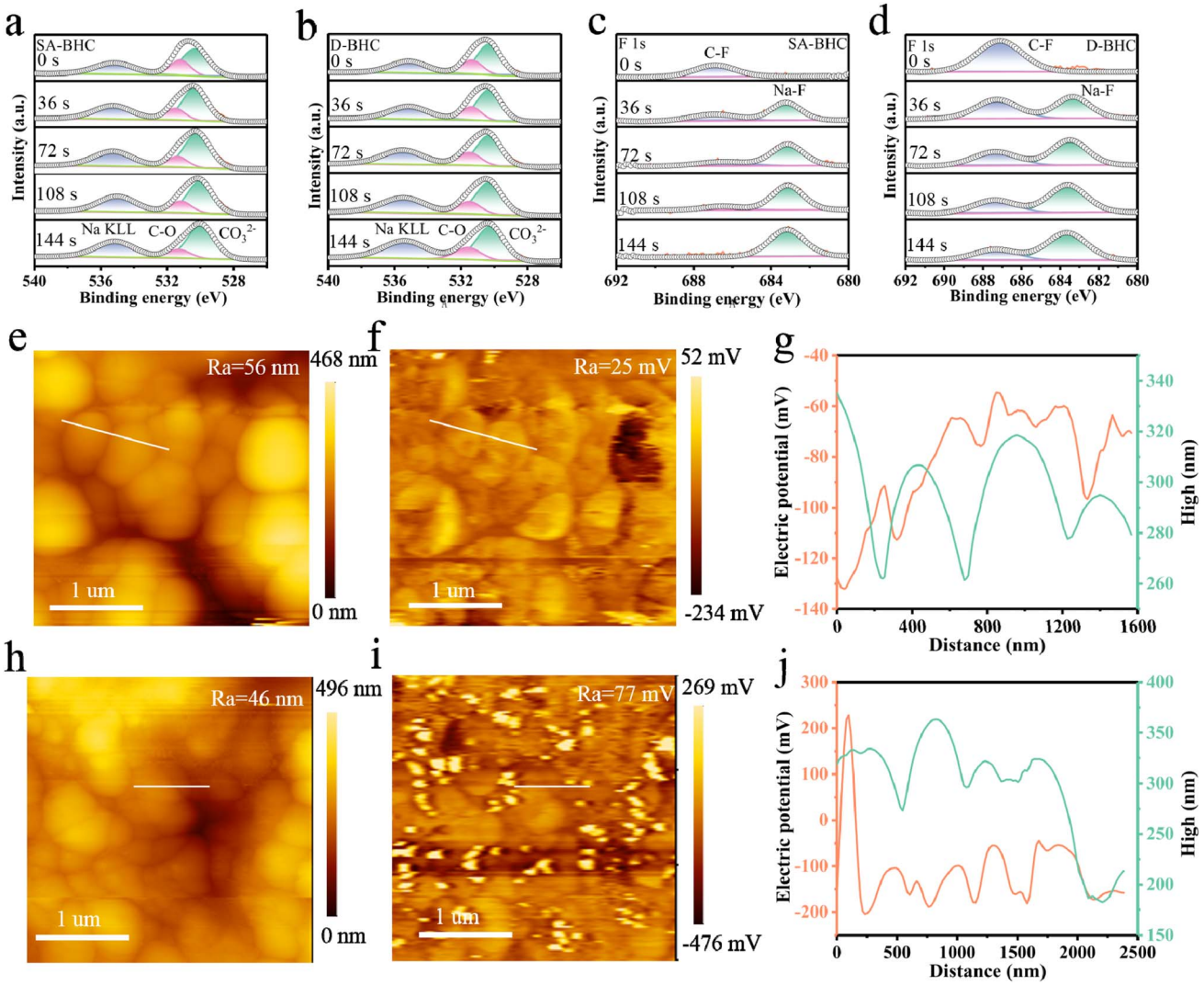

Fig. 6 Depth-resolved XPS spectra of cycled electrodes: (a and b) O 1s spectra of SA-BHC (a) and D-BHC (b); (c and d) F 1s spectra of SA-BHC (c) and D-BHC (d). KPFM characterization after 500 cycles: (e) topography of SA-BHC; (f) surface potential map; (g) correlated line profiles of surface potential and topography. (h) Topography of D-BHC; (i) surface potential map; (j) correlated line profiles of surface potential and topography.

(Fig. 6a–d). Since inorganic-rich SEI phases such as NaF and Na_2O are commonly associated with higher mechanical robustness and more favorable Na^+ transport across the interface, this compositional trend is consistent with the lower interfacial impedance and improved cycling stability observed for SA-BHC.[52–54] Conversely, the stronger signals associated with organic decomposition products in D-BHC suggest a more organic-dominated interphase and more severe continuous electrolyte degradation, which can increase interfacial resistance and contribute to inferior electrochemical performance.[55]

Kelvin probe force microscopy (KPFM) was further employed to correlate interphase chemistry with surface potential characteristics (Fig. 6e–j). The two electrodes show comparable surface topography/roughness, yet markedly different surface potential distributions: the average contact potential difference (VCPD) of SA-BHC is ~25 mV, whereas that of D-BHC reaches ~77 mV. In KPFM, V_{CPD} reflects the work-function difference between the tip and the sample, $V_{CPD} = (\Phi_{tip} - \Phi_{sample})/e$. While the measured V_{CPD} can be influenced by multiple factors (*e.g.*, interphase composition, local dipoles, and charge distribution), the substantially lower VCPD and more homogeneous potential landscape of SA-BHC are consistent with a more uniform and inorganic-enriched SEI layer. This observation agrees with the depth-resolved XPS and TOF-SIMS results, collectively supporting that an inorganic-dominated, compact SEI contributes to reduced interfacial polarization, improved Na^+ transport, and enhanced electrochemical stability. It should be noted that although D-BHC, H-BHC, and SA-BHC were tested in the same electrolyte, their distinct SEI characteristics mainly originate from differences in specific surface area, oxygen-containing functional groups, and pore connectivity. The moderate surface area, high oxygen content, and interconnected mesoporous channels of SA-BHC favor the formation of a thin, inorganic-rich SEI, whereas the high surface area and open porosity of D-BHC promote excessive electrolyte decomposition and the formation of a thick, organic-dominated interphase.

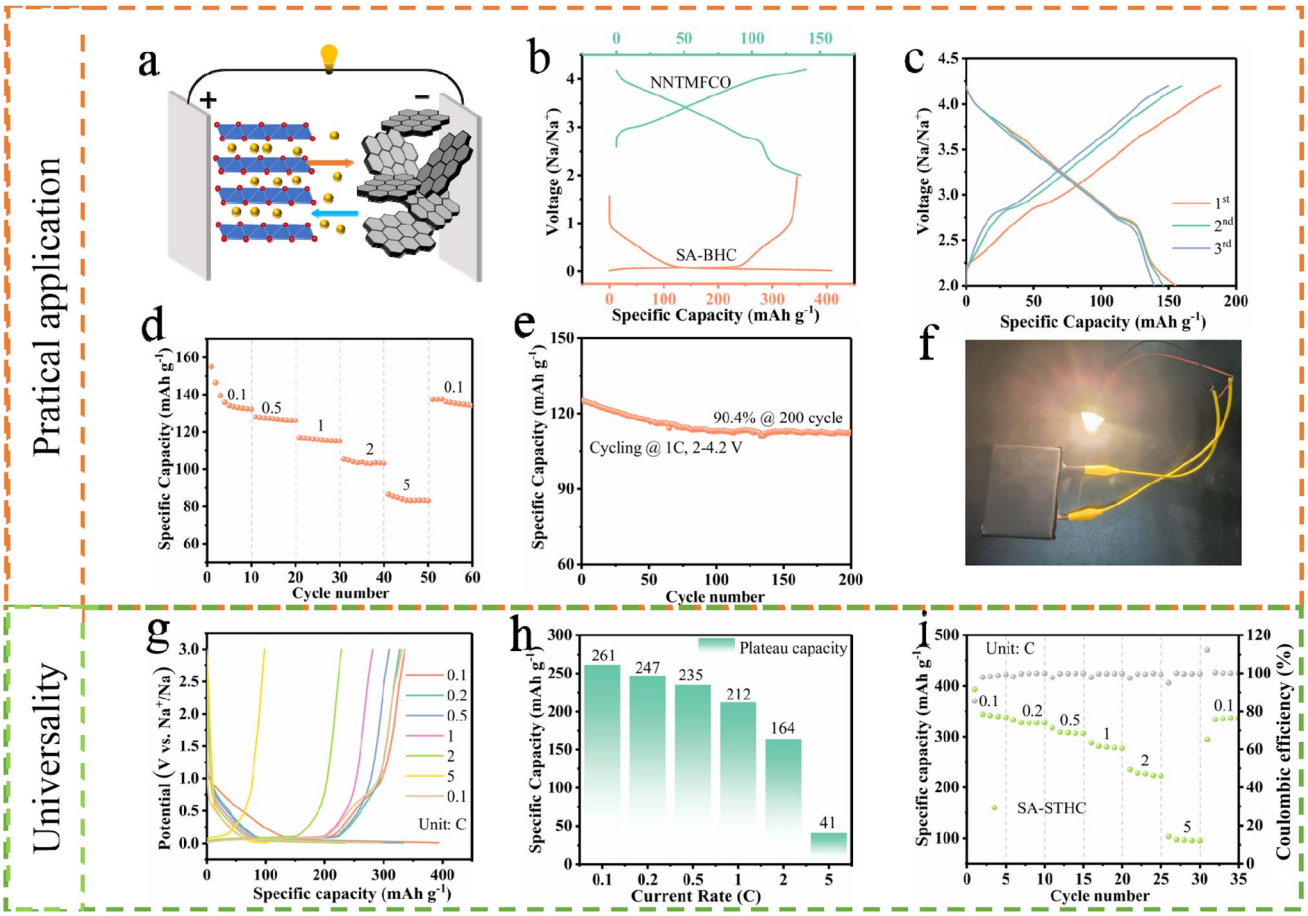

Fig. 7 (a) Schematic of the NNTMFCO||SA-BHC pouch-type full cell. (b) Capacity matching between the SA-BHC anode and NNTMFCO cathode. (c) Charge–discharge profiles of the NNTMFCO||SA-BHC pouch cell at 0.1C. (d) Rate capability from 0.1 to 5C. (e) Cycling performance at 1C. (f) Photograph of a yellow LED powered by the NNTMFCO||SA-BHC pouch cell. (g) GCD profiles of SA-STHC at 0.1–5C. (h) Plateau capacity of HC-Starch at 0.1–5C. (i) Rate performance of SA-STHC.

To demonstrate practical feasibility, we assembled a pouch-type full cell using SA-BHC as the anode and the layered oxide $NaNi_{0.3}Mn_{0.4}Fe_{0.1}Co_{0.1}Ti_{0.1}O_2$ (NNTMFCO) as the cathode (Fig. 7a and b). Galvanostatic charge–discharge tests within 2.0–4.2 V show limited polarization and a small irreversible capacity loss (Fig. 7c), indicating efficient charge transfer and stable interphase behavior under full-cell conditions. The pouch cell delivers reversible specific capacities of 133.1, 126.9, 115.8, 103.8, and 83.4 mA h g^{-1} at 0.1, 0.5, 1, 2, and 5C, respectively, demonstrating robust rate capability (Fig. 7d). Furthermore, after 200 cycles at 1C, the cell retains 90.4% of its capacity (Fig. 7e), confirming good cycling stability. As a direct proof-of-concept, the assembled pouch cell is able to power an LED bulb (Fig. 7f), further supporting its practical applicability.

To examine the general applicability of the molecular-templating liquid-phase carbonization strategy, the same synthetic protocol was extended to another biomass precursor, namely starch, yielding a hard carbon sample denoted as SA-STHC. To further verify the generality of this strategy, true-density measurements were carried out on SA-STHC. The SA-STHC sample exhibits a true density of 1.66 g cm^{-3}, which is substantially lower than that of D-STHC (1.89 g cm^{-3}), thereby confirming the formation of abundant closed nanopores (Fig. S23). As shown in Fig. 7g–i, HC-Starch delivers a reversible capacity of 346 mA h g^{-1} at 0.1C and maintains a plateau capacity of 41 mA h g^{-1} even at 5C, indicating that the strategy consistently promotes the formation of effective confined storage sites and preserves low-voltage capacity under high-rate conditions. In addition, HC-Starch sustains 164 mA h g^{-1} at 2C, comparing favorably with most reported starch-derived HC. These results collectively verify that molecular-templating liquid-phase precursor engineering provides a broadly applicable route to regulate pore architectures across different biomass systems, offering a practical design principle for high-performance HC anodes.

3. Conclusions

In this work, we establish a molecular-templating liquid-phase carbonization strategy to engineer biomass-derived HC toward high closed-pore utilization, addressing a key bottleneck for low-voltage plateau capacity in sodium-ion batteries. Sodium acetate treatment introduces abundant oxygen-containing motifs (C=O/C–O and ester-related functionalities) and

molecular-scale "pre-pores" in bamboo precursors. Upon high-temperature carbonization, these programmed features evolve into a hierarchical architecture comprising size-matched ultramicropores (<0.8 nm) and percolating transport pathways, while maintaining an expanded interlayer spacing (d_{002} = 0.391 nm). This architecture transforms closed pores from "present" to "accessible", enabling a high closed-pore utilization of 86% and promoting the formation of a thin, inorganic-enriched SEI. As a result, the optimized SA-BHC delivers a high reversible capacity of 369 mA h g^{-1} at 0.1C with an ICE of 88.9%, retains 280 mA h g^{-1} after 500 cycles at 2C, and maintains 73% of its room-temperature capacity at −20 °C. Beyond half-cell metrics, the SA-BHC||NNTMFCO pouch full cell demonstrates practical promise, achieving 90.4% capacity retention after 200 cycles at 1C along with good rate capability. Importantly, extending the same protocol to starch-derived HC confirms the generality of this precursor-engineering concept across biomass systems. This work establishes a scalable molecular-level design principle of high-energy hard-carbon anodes for sodium-ion batteries.

Author contributions

Rui Li: conceptualization, visualization, methodology, writing – original draft. Beilei Yuan: investigation, visualization. Yupeng Feng: conceptualization, visualization. Yuhan Li: visualization. Na Jiang: validation. Ping Liu: formal analysis, validation. Liangzhi Li: formal analysis, validation. Weiyue Li: formal analysis, validation. Chunwei Dong: supervision, validation. Shuchun Hu: validation. Qi Liu: formal analysis. Jian Chen: funding acquisition, project administration. Fei Li: visualization, methodology. Jianping Long: supervision, funding acquisition. Anjun Hu: writing – review & editing, funding acquisition, project administration.

Conflicts of interest

The authors declare that they have no known competing financial interests or personal relationships that could have appeared to influence the work reported in this paper.

Data availability

The data supporting this article have been included as part of the supplementary information (SI). Supplementary information is available. See DOI: https://doi.org/10.1039/d6sc01648k.

Acknowledgements

This work was supported by the National Natural Science Foundation of China (52402226 and 52272042), the Key Laboratory of Sichuan Province for Lithium Resources Comprehensive Utilization and New Lithium Based Materials for Advanced Battery Technology (LRMKF202405), the Key Development Projects of the Sichuan Provincial Science and Technology Plan (2022YFG0135) and the Opening Project of Material Corrosion and Protection Key Laboratory of Sichuan province (2025CL03 and 2024CL11).

References

1 J. F. Ruan, J. M. Hu, Q. Li, S. N. Luo, J. Y. Yang, Y. Liu, Y. Song, S. Y. Zheng, D. L. Sun, F. Fang and F. Wang, *Nat. Sustain.*, 2025, **8**, 530–541, DOI: 10.1038/s41893-025-01545-5.
2 Y. Q. Li, A. Vasileiadis, Q. Zhou, Y. X. Lu, Q. S. Meng, Y. Li, P. Ombrini, J. B. Zhao, Z. Chen, Y. S. Niu, X. G. Qi, F. Xie, R. V. D. Jagt, S. Ganapathy, M. M. Titirici, H. Li, L. Q. Chen, M. Wagemaker and Y. S. Hu, *Nat. Energy*, 2024, **9**, 134–142, DOI: 10.1038/s41560-024-01459-0.
3 Z. Y. Lu, H. J. Yang, Y. Guo, H. X. Lin, P. Z. Shan, S. C. Wu, P. He, Y. Yang, Q. H. Yang and H. S. Zhou, *Nat. Commun.*, 2024, **15**, 3497, DOI: 10.1038/s41467-024-47522-y.
4 Y. B. Zhang, S. W. Zhang, Y. Chu, J. Zhang, H. Y. Xue, Y. R. Jia, T. F. Cao, D. Qiu, X. L. Zou, D. W. Wang, Y. Tao, G. M. Zhong, Z. Q. Peng, F. Y. Kang, W. Lv and Q. H. Yang, *Nat. Commun.*, 2025, **16**, 3634, DOI: 10.1038/s41467-025-59022-8.
5 C. W. Lee, S. E. Jun, S. J. Kim, T. H. Lee, S. A. Lee, J. W. Yang, J. H. Cho, S. Choi, C. Kim, S. Y. Kim and H. W. Jang, *Infomat*, 2023, **5**, e12427, DOI: 10.1002/inf2.12427.
6 Y. Chu, J. Zhang, Y. B. Zhang, Q. Li, Y. R. Jia, X. M. Dong, J. Xiao, Y. Tao and Q. H. Yang, *Adv. Mater.*, 2023, **35**, 2212186, DOI: 10.1002/adma.202212186.
7 F. Wang, L. Chen, J. Q. Wei, C. Z. Diao, F. Li, C. C. Du, Z. S. Bai, Y. Y. Zhang, O. I. Malyi, X. D. Chen, Y. X. Tang and X. J. Bao, *Energy Environ. Sci.*, 2025, **18**, 4312–4323, DOI: 10.1039/D5EE00104H.
8 J. J. Liu, Y. W. You, L. Huang, Q. Z. Zheng, Z. F. Sun, K. Fang, L. Y. Sha, M. Liu, X. Zhan, J. B. Zhao, Y. C. Han, Q. B. Zhang, Y. N. Chen, S. Q. Wu and L. Zhang, *Adv. Mater.*, 2024, **36**, 2407369, DOI: 10.1002/adma.202407369.
9 Y. Q. Li, Y. X. Lu, P. Adelhelm, M. M. Titirici and Y. S. Hu, *Chem. Soc. Rev.*, 2019, **48**, 4655–4687, DOI: 10.1039/C9CS00162J.
10 D. Saurel, B. Orayech, B. W. Xiao, D. Carriazo, X. L. Li and T. Rojo, *Adv. Energy Mater.*, 2018, **8**, 1703268, DOI: 10.1002/aenm.201703268.
11 S. Alvin, H. S. Cahyadi, J. Hwang, W. Chang, S. K. Kwak and J. Kim, *Adv. Energy Mater.*, 2020, **10**, 2000283, DOI: 10.1002/aenm.202000283.
12 H. Au, H. Alptekin, A. C. S. Jensen, E. Olsson, C. A. O'Keefe, T. Smith, M. C. Ribadeneyra, T. F. Headen, C. P. Grey, Q. Cai, A. J. Drew and M. M. Titirici, *Energy Environ. Sci.*, 2020, **13**, 3469–3479, DOI: 10.1039/d0ee01363c.
13 X. X. He, W. H. Lai, Y. Liang, J. H. Zhao, Z. Yang, J. Peng, X. H. Liu, Y. X. Wang, Y. Qiao, L. Li, X. Q. Wu and S. L. Chou, *Adv. Mater.*, 2023, **35**, 2302613, DOI: 10.1002/adma.202302613.
14 S. H. Xiao, Y. J. Guo, H. X. Chen, H. Z. Liu, Z. Q. Lei, L. B. Huang, R. X. Jin, X. C. Su, Q. Y. Zhang and Y. G. Guo, *Adv. Mater.*, 2025, **37**, 2501434, DOI: 10.1002/adma.202501434.
15 H. Kim, J. C. Hyun, D. H. Kim, J. H. Kwak, J. B. Lee, J. H. Moon, J. Choi, H. D. Lim, S. J. Yang, H. M. Jin, D. J. Ahn, K. Kang, H. J. Jin, H. K. Lim and Y. S. Yun, *Adv. Mater.*, 2023, **35**, 2209128, DOI: 10.1002/adma.202209128.

16 C. N. Li, Q. N. Chen, Y. H. Zhang, P. D. Zhao, X. X. He, Q. F. Gu, J. Z. Wang, S. L. Chou and X. Q. Wu, *Energy Storage Mater.*, 2025, **82**, 104580, DOI: 10.1016/j.ensm.2025.104580.
17 L. Z. Xu, J. X. Chen, D. G. Liu, K. Zhao, T. T. Liu, L. Huang, S. Y. Hu, T. Q. Yin, T. Zhang, J. Song, Z. L. Wu, C. Li and Y. Fu, *J. Am. Chem. Soc.*, 2026, **148**, 12849–12860, DOI: 10.1021/jacs.5c21030.
18 W. J. Huang, C. Wu, L. Zhong, Q. H. Chen, H. Zhang, X. Tan, S. L. Chou and X. Q. Wu, *Adv. Energy Mater.*, 2023, **16**, e05568, DOI: 10.1002/aenm.202505568.
19 L. K. Iglesias, E. N. Antonio, T. D. Martinez, L. Zhang, Z. Q. Zhuo, S. J. Weigand, J. H. Guo and M. F. Toney, *Adv. Energy Mater.*, 2023, **13**, 2302171, DOI: 10.1002/aenm.202302171.
20 N. Sun, J. S. Qiu and B. Xu, *Adv. Energy Mater.*, 2022, **12**, 2200715, DOI: 10.1002/aenm.202200715.
21 Z. Y. Guo, Z. Xu, F. Xie, J. L. Jiang, K. Zheng, S. Alabidun, M. Crespo-Ribadeneyra, Y. S. Hu, H. Au and M. M. Titirici, *Adv. Mater.*, 2023, **35**, 2304091, DOI: 10.1002/adma.202304091.
22 J. Z. Yang, Q. J. Ren, Z. Y. Sun, J. Wang, R. R. Hao and Z. Q. Shi, *Energy Storage Mater.*, 2025, **82**, 104574, DOI: 10.1016/j.ensm.2025.104574.
23 J. Wang, L. Yan, B. H. Liu, Q. J. Ren, L. L. Fan, Z. Q. Shi and Q. Y. Zhang, *Chin. Chem. Lett.*, 2023, **34**, 107526, DOI: 10.1016/j.cclet.2022.05.040.
24 Y. F. Chen, H. Y. Sun, X. X. He, Q. H. Chen, J. H. Zhao, Y. H. Wei, X. Q. Wu, Z. J. Zhang, Y. Jiang and S. L. Chou, *Small*, 2024, **20**, 2307132, DOI: 10.1002/smll.202307132.
25 D. Sun, L. Zhao, P. L. Sun, K. Zhao, Y. K. Sun, Q. Zhang, Z. C. Li, Z. Ma, F. Z. Zheng, Y. Yang, C. B. Lu, C. Peng, C. M. Xu, Z. H. Xiao and X. L. Ma, *Adv. Funct. Mater.*, 2024, **34**, 2403642, DOI: 10.1002/adfm.202403642.
26 Z. X. Lu, J. Wang, W. L. Feng, X. P. Yin, X. C. Feng, S. Y. Zhao, C. X. Li, R. X. Wang, Q. A. Huang and Y. F. Zhao, *Adv. Mater.*, 2023, **35**, 2211461, DOI: 10.1002/adma.202211461.
27 K. F. Wang, F. Sun, H. Wang, D. Y. Wu, Y. X. Chao, J. H. Gao and G. B. Zhao, *Adv. Funct. Mater.*, 2022, **32**, 2203725, DOI: 10.1002/adfm.202203725.
28 Z. Y. Liu, X. Wang, X. Xie, Y. Li, H. Peng, G. F. Ma and Z. Q. Lei, *J. Energy Chem.*, 2026, **112**, 1–12, DOI: 10.1016/j.jechem.2025.08.038.
29 Z. H. Chen, J. L. Shen, W. J. Deng, Y. S. Huang, P. Z. Shan, Y. H. Lou, L. Li, G. Y. Gao, Y. X. Yang, S. N. He, H. G. Pan, X. H. Rui, Y. Yang, H. Yang and Y. Yu, *Natl. Sci. Rev.*, 2025, **13**, nwaf566, DOI: 10.1093/nsr/nwaf566.
30 L. B. Wang, Z. K. Xu, P. Lin, Y. Zhong, X. L. Wang, Y. F. Yuan and J. P. Tu, *Adv. Energy Mater.*, 2025, **15**, 2403084, DOI: 10.1002/aenm.202403084.
31 C. Wu, Y. R. Yang, Y. F. Li, X. X. He, Y. H. Zhang, W. J. Huang, Q. H. Chen, X. H. Liu, S. Q. Chen, Q. F. Gu, L. Li, S. C. Smith, X. Tan, Y. Yu, X. Q. Wu and S. Chou, *Energy Environ. Sci.*, 2025, **18**, 6019–6031, DOI: 10.1039/d5ee00278h.
32 M. X. Song, L. J. Xie, F. Y. Su, Z. L. Yi, Q. G. Guo and C. M. Chen, *Chin. Chem. Lett.*, 2024, **35**, 109266, DOI: 10.1016/j.cclet.2023.109266.
33 S. Y. Li, H. T. Yin, Z. W. Xing, X. C. Lin, J. C. Liu and R. P. Liu, *Angew. Chem., Int. Ed.*, 2025, **64**, e202512936, DOI: 10.1002/anie.202512936.
34 Q. H. Chen, Q. X. Wen, C. Li, C. C. Li, P. D. Zhao, L. Li, X. Tan, J. Z. Wang, X. L. Fan, S. L. Chou and X. Q. Wu, *Adv. Mater.*, 2025, e15495, DOI: 10.1002/adma.202515495.
35 R. Li, B. R. Yang, A. J. Hu, B. Zhou, M. J. Liu, L. Yang, Z. F. Yan, Y. N. Fan, Y. Pan, J. H. Chen, T. Li, K. Li, J. Liu and J. P. Long, *Carbon*, 2023, **215**, 118489, DOI: 10.1016/j.carbon.2023.118489.
36 R. Li, A. J. Hu, Z. Wang, W. Yang, Q. He, W. Y. Li, L. Z. Li, W. Jiao, B. L. Yuan, J. Chen, F. Li and J. P. Long, *J. Energy Chem.*, 2026, **112**, 832–841, DOI: 10.1016/j.jechem.2025.08.091.
37 R. Li, C. B. Su, W. Xu, W. Yang, J. Chen, J. P. Long and A. J. Hu, *ChemSusChem*, 2025, **18**, e202501384, DOI: 10.1002/cssc.202501384.
38 R. Li, C. B. Su, W. Yang, R. Z. Xu, K. Chen, J. Chen, W. Su, B. L. Yuan, J. P. Long and A. J. Hu, *Chem. Eng. J.*, 2025, **506**, 159968, DOI: 10.1016/j.cej.2025.159968.
39 Y. Y. Peng, Y. H. Fu, M. M. Yu, L. Zhao, H. Z. Zeng, S. T. Niu, J. Zhang, J. L. Chen, G. Liu, Y. Z. Wu and F. Ran, *Susmat*, 2024, **4**, e217, DOI: 10.1002/sus2.217.
40 Y. L. Wang, Z. L. Yi, L. J. Xie, Y. X. Mao, W. J. Ji, Z. J. Liu, X. X. Wei, F. Y. Su and C. M. Chen, *Adv. Mater.*, 2024, **36**, 401249, DOI: 10.1002/adma.202401249.
41 A. Agrawal, S. Janakiraman, K. Biswas, A. Venimadhav, S. K. Srivastava and S. Ghosh, *Electrochim. Acta*, 2019, **317**, 164–172, DOI: 10.1016/j.electacta.2019.05.158.
42 D. T. Ma, Y. L. Li, H. W. Mi, S. Luo, P. X. Zhang, Z. Q. Lin, J. Q. Li and H. Zhang, *Angew. Chem., Int. Ed.*, 2018, **57**, 8901–8905, DOI: 10.1002/anie.201802672.
43 J. H. Pan, Z. F. Sun, X. Y. Wu, T. C. Liu, Y. R. Xing, J. W. Chen, Z. C. Xue, D. F. Tang, X. L. Dong, H. T. Zhang, H. D. Liu, Q. L. Wei, D. L. Peng, K. Amine and Q. B. Zhang, *J. Am. Chem. Soc.*, 2025, **147**, 3047–3061, DOI: 10.1021/jacs.4c09824.
44 S. J. Jiang, Y. S. Xu, X. W. Sun, L. Chen, Y. N. Li, L. Li and F. F. Cao, *J. Am. Chem. Soc.*, 2025, **147**, 8088–8092, DOI: 10.1021/jacs.4c15593.
45 D. Q. Chen, K. Y. Luo, Z. W. Yang, Y. J. Zhong, Z. G. Wu, Y. Song, G. Chen, G. K. Wang, B. H. Zhong and X. D. Guo, *Carbon*, 2021, **173**, 253–261, DOI: 10.1016/j.carbon.2020.11.004.
46 Y. M. Li, Y. S. Hu, X. G. Qi, X. H. Rong, H. Li, X. J. Huang and L. Q. Chen, *Energy Storage Mater.*, 2016, **5**, 191–197, DOI: 10.1016/j.ensm.2016.07.006.
47 S. F. Huang, Z. P. Li, B. Wang, J. J. Zhang, Z. Q. Peng, R. J. Qi, J. Wang and Y. F. Zhao, *Adv. Funct. Mater.*, 2018, **28**, 1706294, DOI: 10.1002/adfm.201706294.
48 T. Li, A. J. Hu, Y. J. Li, B. R. Yang, K. Li, K. Chen, J. Y. Jiang, F. Li, Z. W. Seh, J. Wang and J. P. Long, *Adv. Funct. Mater.*, 2025, **35**, 2507310, DOI: 10.1002/adfm.202507310.
49 K. Chen, A. J. Hu, W. Yang, Y. J. Li, Z. W. Seh, F. Li, J. P. Long and S. Chen, *Adv. Funct. Mater.*, 2025, e13143, DOI: 10.1002/adfm.202513143.

50 W. Xu, A. J. Hu, R. X. Zheng, Y. J. Li, K. Chen, J. Z. Chen, Z. Wang, R. Z. Xu, J. Wang, F. Li, J. P. Long and F. X. Wu, *Adv. Funct. Mater.*, 2025, **36**, e11135, DOI: 10.1002/adfm.202511135.

51 R. Z. Xu, A. J. Hu, W. Xu, W. Yang, F. Li, Y. J. Li, Y. B. Mu, L. Zeng, J. P. Long and S. M. Chen, *Angew. Chem., Int. Ed.*, 2025, **64**, e202513321, DOI: 10.1002/anie.202513321.

52 W. Xu, Y. Y. Yin, A. J. Hu, Y. J. Li, J. Wang, J. P. Long, L. Zeng and S. M. Chen, *Energy Environ. Sci.*, 2026, **19**, 384–396, DOI: 10.1039/d5ee04892c.

53 B. R. Yang, Y. K. Wang, R. X. Zheng, W. Yang, Y. J. Li, T. Li, K. Li, A. J. Hu, J. P. Long and S. J. Ding, *Angew. Chem., Int. Ed.*, 2025, **64**, e202508486, DOI: 10.1002/anie.202508486.

54 J. Z. Chen, Y. D. Qian, Y. Y. Yin, Y. J. Hu, H. L. Chen, Y. Xu, X. Zhang, Y. P. Feng, J. Y. Tian, Y. J. Li, X. H. Ren, H. Zhang, Q. Liu, J. P. Long and A. J. Hu, *Energy Storage Mater.*, 2025, **84**, 104835, DOI: 10.1016/j.ensm.2025.104835.

55 S. S. Chen, Y. Wang, Z. X. Li, Y. Y. Feng and W. Feng, *J. Mater. Chem. A*, 2024, **12**, 28296–28306, DOI: 10.1039/d4ta04343j.